

# Reduction of blob-filament radial propagation by parallel variation of flows: analysis of a gyrokinetic simulation

J. R. Myra,<sup>1</sup> S. Ku,<sup>2</sup> D.A. Russell,<sup>1</sup> J. Cheng,<sup>3</sup> I. Keramidias Charidakos,<sup>3,4</sup>  
S. E. Parker,<sup>3</sup> R.M. Churchill,<sup>2</sup> and C.S. Chang<sup>2</sup>

<sup>1</sup> *Lodestar Research Corporation, 2400 Central Avenue, Boulder, CO 80301, USA*

<sup>2</sup> *Princeton Plasma Physics Laboratory, Princeton, NJ 08543, USA*

<sup>3</sup> *Department of Physics, University of Colorado, Boulder, CO 80309, USA*

<sup>4</sup> *Present address: Los Alamos National Laboratory, Los Alamos, NM 87544, USA*

April 2020  
revised July 2020

accepted for publication in  
*Physics of Plasmas*

---

PPPL/SO15882-3

LRC-20-185

---

**LODESTAR RESEARCH CORPORATION**  
2400 Central Avenue  
Boulder, Colorado 80301

# Reduction of blob-filament radial propagation by parallel variation of flows: analysis of a gyrokinetic simulation

J. R. Myra,<sup>1,a)</sup> S. Ku,<sup>2</sup> D.A. Russell,<sup>1</sup> J. Cheng,<sup>3</sup> I. Keramidis Charidakos,<sup>3,4</sup>  
S. E. Parker,<sup>3</sup> R.M. Churchill,<sup>2</sup> and C.S. Chang<sup>2</sup>

<sup>1</sup> *Lodestar Research Corporation, 2400 Central Avenue, Boulder, CO 80301, USA*

<sup>2</sup> *Princeton Plasma Physics Laboratory, Princeton, NJ 08543, USA*

<sup>3</sup> *Department of Physics, University of Colorado, Boulder, CO 80309, USA*

<sup>4</sup> *Present address: Los Alamos National Laboratory, Los Alamos, NM 87544, USA*

## ***Abstract***

Data from the XGC1 gyrokinetic simulation is analyzed to understand the three-dimensional spatial structure and the radial propagation of blob-filaments generated by quasi-steady turbulence in the tokamak edge pedestal and scrape-off layer plasma. Spontaneous toroidal flows vary in the poloidal direction and shear the filaments within a flux surface resulting in a structure that varies in the parallel direction. This parallel structure allows the curvature and grad-B induced polarization charge density to be shorted out via parallel electron motion. As a result, it is found that the blob-filament radial velocity is significantly reduced from estimates which neglect parallel electron kinetics, broadly consistent with experimental observations. Conditions for when this charge shorting effect tends to dominate blob dynamics are derived and compared with the simulation.

Keywords: blob, filament, gyrokinetic, electron dynamics, simulation, sheared flow

a) Author to whom correspondence should be addressed: jrmya@lodestar.com

# I. Introduction

Blob-filaments<sup>1-3</sup> (also called blobs, filaments, intermittent plasma objects, coherent structures) have a long history of research in plasma physics, dating from observations in the 1980s,<sup>4</sup> to present magnetic fusion devices.<sup>5-10</sup> These coherent structures are of interest for fusion research in that they, or the turbulence from which they emerge, may influence the near-SOL (scrape-off layer) width<sup>11-17</sup> as well as mid to far-SOL profiles<sup>18-21</sup> and main chamber wall interactions.

The importance of, and intrinsic interest in, blob-filaments has spawned considerable theoretical efforts to understand blob radial velocities<sup>2,3,22-25</sup> Originally carried out in model two-dimensional geometries using fluid theory,<sup>26-29</sup> the models were later extended to three dimensions,<sup>30-32</sup> and a number of fluid simulation codes now also incorporate increasingly realistic tokamak geometry.<sup>33-36</sup> Recently, kinetic simulation codes have also addressed blob-related research.<sup>37-40</sup> In the present paper, we will continue this thrust by exploring results from the XCG1 code,<sup>41,42</sup> a full-f, 5D particle-in-cell (PIC) gyrokinetic code.

The goal of this paper is to analyze and interpret XGC1 simulation results impacting blob dynamics. In particular we will explore the effect of toroidal flows which vary in the poloidal (parallel) direction on the parallel structure of blob-filaments and the consequences of this imposed structure for radial blob propagation. Thus, the sheared flows considered here are different from the radial variation of poloidal or toroidal flows that have usually been considered in the literature. However, in a broader sense, our work is at least conceptually related to a very large body of work on the effect of sheared flows on plasma turbulence.<sup>43-45</sup> More specifically, it has been observed experimentally that blob-filaments are distorted, and sometimes even split, by the sheared flows that arise from radio-frequency induced convective cells in the SOL.<sup>46</sup> Recently, the effects of sheared poloidal flows on disconnection of blob-filaments from the divertor has been studied.<sup>47</sup>

The plan of our paper is as follows. In Sec. II an overview is presented of the gyrokinetic simulation on which the subsequent analysis is based. This section discusses the magnetic geometry, bulk plasma parameters and the fluctuation statistics. A field line following coordinate system, essential to the filament analysis, is introduced in Sec. III A, followed in Sec. III B by the simulation results for blob-filament structure and motion.

The theory of charge shorting by parallel electron motion is discussed in Sec. IV. Charge shorting occurs when curvature and grad-B induced polarization charges, responsible for blob-filament radial convection, are mitigated by the parallel electron conduction. A heuristic condition for shorting is given for a collisionless system in Sec. IV A, and this result is compared to and reconciled with a similar condition that applies in a collisional fluid model in Sec. IV B.

In Sec. V, the theory is applied to the blob-filaments observed in the simulation. It is shown that they are in the collisionless regime and that they satisfy the condition required for charge shorting. Furthermore, the density and potential fluctuations in the simulation are shown to be nearly in phase, consistent with the dominant role of electron parallel conductivity. Several diagnostic methods were applied to the simulation to measure the radial velocity of the blob-filaments. The blob-filament velocity was found to be smaller than that expected from an ideal analytical estimate that ignores the charge shorting mechanism.

A discussion of some related points is given in Sec. VI and a summary of the paper and the main conclusions are given in Sec. VII. Three additional topics are discussed in appendices. Appendix A provides details of the time-lag correlation method used to measure blob-filament motion, Appendix B discusses the blob-velocity proxy method and Appendix C discusses various regimes of the two-region blob model with respect to the simulation.

In our paper the terms blob-filament, blob and filament will be used almost interchangeably, the choice depending on whether the particular emphasis of the discussion is on perpendicular (blob) or parallel (to B, filament) structure.

## II. Simulation overview

In this paper we analyze an XGC1 simulation of the lower single null Alcator C-Mod EDA high (H) mode discharge #1160930033 with plasma current  $I_p = 1.4$  MA, toroidal magnetic field 5.4 T, input power 5.4 MW and record volume averaged pressure exceeding 0.2 MPa.<sup>48</sup> The geometry is shown in Fig. 1. In addition to the active lower X-point, there is a “virtual” upper X-point, i.e. an X-point outside the analyzed simulation domain whose effect on the near-separatrix geometry is still important. The ion grad-B drift is directed downwards, towards the (lower) X-point.

The simulation was initialized with experimental profiles of density and temperature and reconstructed (kinetic EFIT) magnetic equilibrium. This electrostatic simulation employs drift kinetic electrons and gyrokinetic ions. It implements a logical sheath boundary condition<sup>49</sup> at the

divertor plate (which sets the plasma potential such that electrons with lower parallel velocity are reflected in sufficient numbers to maintain ambipolarity). Two neutral-plasma interaction models are available within XGC1, a built-in model which only treats atoms, and an interface to the more sophisticated DEGAS2 Monte Carlo neutral transport code. The former model is used in the present work and is described in detail elsewhere.<sup>50</sup> Only half of the toroidal extent of the device was simulated; the rest was reconstructed using periodicity so that only even toroidal mode numbers are present in the simulation. The XGC1 code employs an unstructured mesh in the  $(R, Z)$  plane with spatially varying resolution., and this simulation used  $N_\zeta = 16$  toroidal, i.e.  $(R, Z)$ , planes in the half-torus simulation.

Although the simulation encompasses the whole  $(R, Z)$  plane of the torus, albeit with reduced resolution in the interior core, our analysis in this paper is restricted to the edge and SOL region shown in Fig. 1. In the radial direction this analysis domain is defined by normalized poloidal flux in the range  $\psi = (0.97, 1.02)$  where  $\psi = 1$  is the separatrix. This corresponds to a range of distances from the separatrix of  $\Delta R = \pm 4$  mm at the outboard midplane, well short of the distance to the main chamber wall. In Fig. 1, the location of the main chamber first wall is shown for general reference; the study of far SOL blobs and wall interactions is deferred to future work. The first wall at locations with  $\psi < 1.07$  was included in the full simulation. In the region with  $\psi > 1.07$  any turbulent or neoclassical potential perturbations were ignored. Thus, the simulation includes neutral effects in the regions where there are blobs, but the self-consistent blob interaction with the wall is not taken into account because of the radial buffer zone.

In the region of interest for this paper, namely the near-separatrix region, each of the 16 toroidal planes contained  $7.6 \times 10^4$  nodes for a total of over  $1.2 \times 10^6$  nodes. The spatial separation of the nodes is about 0.5 mm which is comparable to the ion gyro-radius at the separatrix. The 16-plane toroidal resolution per half torus is sufficient because the unstructured mesh in the  $(R, Z)$  plane is carefully chosen to place nodes nearly along field lines. Field-line-following (FLF) methods used in the analysis, are discussed in Sec. III A. The toroidal planes end up determining the parallel resolution of the filament, which is slowly varying while the perpendicular resolution is set by the node spacing.

The (deuterium) plasma conditions in the simulation are roughly characterized by the following parameters on the separatrix at the outboard midplane: density  $n_e = 1.3 \times 10^{20} \text{ m}^{-3}$ , electron temperature  $T_e = 127 \text{ eV}$ , ion temperature  $T_i = 203 \text{ eV}$  and magnetic field  $B = 4.4 \text{ T}$ .

The plasma profiles decay rapidly into the SOL. The electron pressure gradient scale length in the near SOL is  $\lambda_p \sim 0.8$  mm.

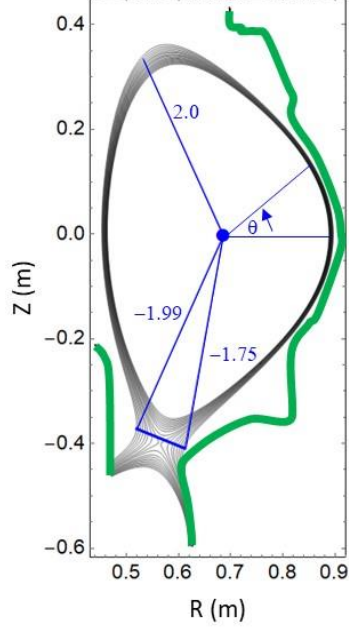


Figure 1. Flux surfaces (black) in the edge and SOL region of the simulation domain in the  $(R, Z)$  plane and vessel walls (green). The angle  $\theta$  is defined to be zero at the outboard midplane. The thick blue line bisecting the X-point is denoted as the X-line. For a given flux surface in the SOL, there is a gap in  $\theta$  corresponding to this line. For the outermost flux surface the gap is for  $-1.99 < \theta < -1.75$ . Analysis in this paper is restricted to the indicated flux surfaces for fluctuations above the X-line, and for  $\theta < 2.0$ , where, as we will see, the dominant blob filaments are confined.

The RMS fluctuation amplitudes peak just outside the separatrix at  $\sim 13\%$  for the relative density fluctuations  $\delta n/\bar{n}$  and  $\sim 20\%$  for the relative potential fluctuation  $e\delta\Phi/T_e$ . Here we define fluctuations as departures from the toroidal ( $\zeta$ ) average, e.g.

$$n = \frac{1}{2\pi} \int d\zeta n + \delta n \equiv \bar{n} + \delta n \quad (1)$$

Individual fluctuations can easily reach 50% in the SOL, and infrequent stronger fluctuations occur, i.e. intermittency is present as expected.

The intermittency properties are illustrated in Fig. 2 which used data in the entire range  $\psi = (0.97, 1.02)$ , poloidal angle  $\theta$  in the range  $(-1.7, 2.0)$  and a swath of toroidal angle  $\sim 0.48$  rad in width. (The statistics are expected to be toroidally axisymmetric.) There is nothing particularly

surprising in Fig. 2; rather, it confirms that this XGC1 simulation recovers standard statistical results for SOL intermittency such as a skewed and asymmetric probability distribution function of amplitudes in Fig. 2(a), a mostly increasing normalized density fluctuation level as one moves from the closed to the SOL flux surfaces in Fig. 2(b), and a density fluctuation skewness that is negative on the closed flux surfaces passes through zero and increases through positive values as one moves in the SOL in Fig. 2(c). The point where the skewness  $S$  is zero has been interpreted as the blob birth location: from this location holes ( $S < 0$ ) move inward while blobs ( $S > 0$ ) move outwards in radius.<sup>2,3</sup> Fluctuations in  $\delta n/\bar{n}$  peak just outside the separatrix near a normalized poloidal flux coordinate value of  $\psi = 1.01$  where much of the blob-filament analysis in this paper will be carried out. This flux surface corresponds to  $\Delta R = 1.5$  mm at the outboard midplane.

### III. Analysis of simulated blob-filaments

#### A. Field line following coordinates

The intermittency illustrated in Fig. 2 is present in coherent structures which emerge from unstable linear modes. These structures, in the form of blob-filaments, are best viewed and analyzed in field line following (FLF) coordinates because of the large disparity in their spatial scales across and along curved field lines. The FLF coordinates used in the paper are the radial coordinate  $\psi$ , the parallel coordinate  $\theta$ , and a toroidal coordinate  $\zeta_\theta$ . An individual field line is labeled by two parameters  $\psi$  and  $\zeta_\theta$  where  $\zeta_\theta$  specifies the toroidal angle of the field line at a reference poloidal location  $\theta_\theta'$ . Here that reference location is taken as the location of the X-line. Thus, the transformation from geometric angle  $(\psi', \theta', \zeta')$  coordinates to FLF  $(\psi, \theta, \zeta_\theta)$  coordinates is defined by

$$\begin{aligned}\psi &= \psi' \\ \theta &= \theta' \\ \zeta_\theta &= \zeta' - \int_{\theta'_0}^{\theta'} d\theta' \frac{B_\zeta}{RB\theta' |\nabla\theta'|}\end{aligned}\tag{2}$$

where the equation of a field line is  $Rd\zeta'/ds = B\zeta/B\theta'$  and  $ds$  is the distance moved in the poloidal direction while moving through  $d\zeta'$  in the toroidal direction. Position along the field line is denoted by  $\theta$  with  $\theta = 0$  corresponding to the outboard midplane and increasing in the counter-

clockwise direction in the  $(R, Z)$  plane, as shown in Fig. 1. The angle  $\theta$  is a geometrical angle referenced to the magnetic axis.

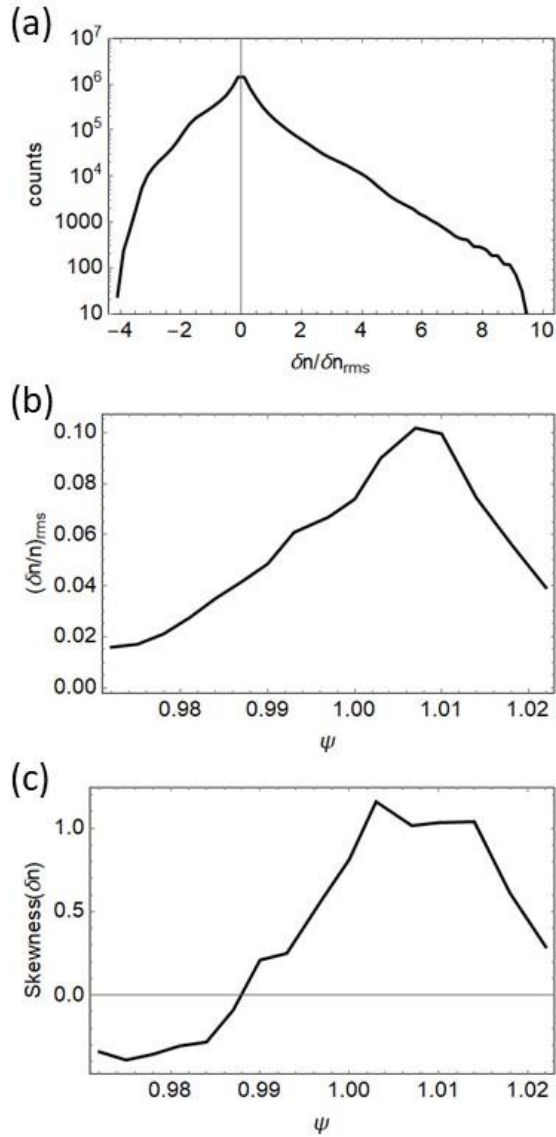


Figure 2. Statistical properties of fluctuations in the XGC1 simulation: (a) Histogram of normalized density fluctuation levels for the edge-SOL domain; (b) RMS density fluctuation amplitude and (c) skewness, both vs. radial coordinate parametrized by the normalized poloidal flux.

Special care is taken in performing the data analysis by using FLF interpolation. First fluctuation data is obtained on each computational mesh node in the  $(R, Z)$  plane for each of the  $N_\zeta = 16$  toroidal planes in the half-torus simulation. We denote these toroidal planes by the

discrete index  $i\zeta = (1, N\zeta)$ . The data is interpolated to create  $N\zeta$  continuous functions of  $\delta n/\bar{n}$ , one for each toroidal plane. The transform to FLF coordinates is then carried out to obtain  $\delta n/\bar{n}$  at an arbitrary value of  $(\psi, \theta, \zeta_0)$  using the following method.

We first note that a given field line  $(\psi, \zeta_0)$  will intersect each toroidal plane  $i\zeta$  at a particular value of  $\theta$  denoted by  $\theta_i$ . We identify the two adjacent toroidal planes  $(i, i+1)$  defined by  $\theta_i < \theta < \theta_{i+1}$ . Finally, we then interpolate *along the field line* to obtain the fluctuation at the desired point  $(\psi, \theta, \zeta_0)$ .

It should be noted parenthetically that a straightforward three-dimensional interpolation of the raw simulation data (i.e. in the form of nodal mesh values of  $R, Z$  on each toroidal plane) yielded unsatisfactory results because of the disparity in the perpendicular and parallel structure of the fluctuations.

### ***B. Blob-filament structure and motion***

An example of a blob-filament structure in FLF coordinates is shown in Fig. 3. At a given time there are many (~50) such filaments in the SOL of the half torus ( $0 < \zeta_0 < \pi$ ) of the simulation. In this FLF plane, the magnetic field lines are vertical lines at fixed  $\zeta_0$  parameterized by  $\theta$ . The blob radius (half-width-half-max of  $\delta n/\bar{n}$ ) in the direction perpendicular to  $B$  is about 1.8 mm or about  $4\rho_i$ . In the parallel direction the filaments extend for about 1m along the outboard side of the torus from near the top of the device to a location slightly above the X-line. Toroidal flows and the shear in those flows have distorted the blob-filaments and possibly contributed to the X-point disconnection.<sup>47</sup> The flow can be visualized from the two illustrated frames in Fig. 3(a) and 3(b), snapshots taken at a time separation of 3.9  $\mu\text{s}$ . (Data was saved every 0.062  $\mu\text{s}$ , thus, there were many other intermediate frames.) The angular velocity may be roughly estimated from these two frames to be about 23 krad/s. This estimate is confirmed and greatly improved upon by the time lag correlation method, as discussed next. Both the time lag correlation method and the blob tracking method discussed in Sec. V were carried out during an interval of 7.9  $\mu\text{s}$  at the end of the 95  $\mu\text{s}$  total simulation time, when the turbulence was in quasi-steady state.

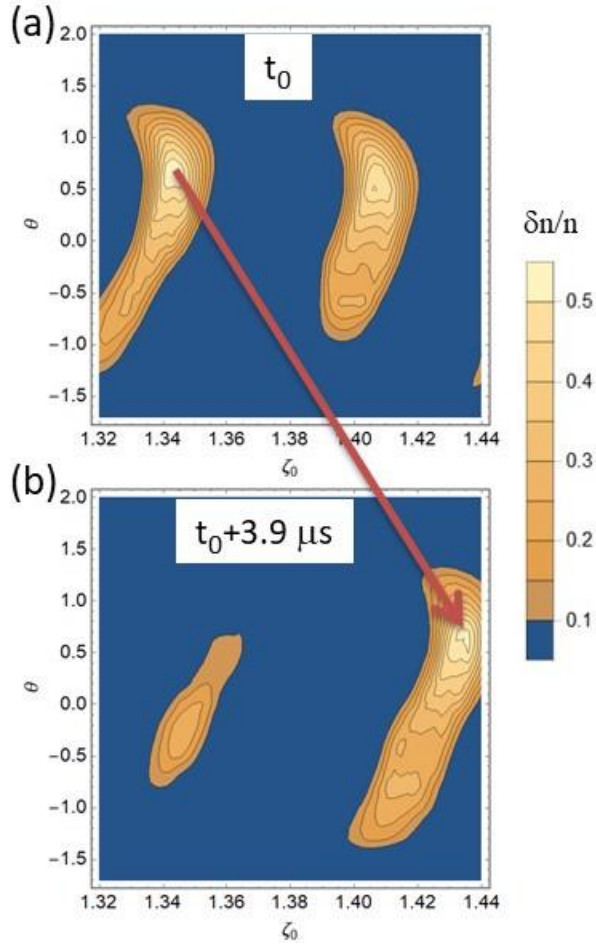


Figure 3. Snapshots showing positive contours of  $\delta n/\bar{n}$  for blob-filaments for a 0.12 radian (6.9 degree) range of toroidal angles on a given flux surface,  $\psi = 1.01$  at two different times: (a) an arbitrary reference time during the quasi-steady turbulent state of the simulation, (b) the same toroidal range 3.9  $\mu\text{s}$  later. The blob is being convected by the toroidal flow. Here  $\theta = -1.7$  is at the X-line,  $\theta = 0$  is the outboard midplane and  $\theta = 2$  is near the top of the machine where there is a virtual X-point. Filled contours of  $\delta n/\bar{n}$  are shown for contour levels 0.1 to 0.5 in steps of 0.1.

The time lag correlation method provides a measure of the velocity of structures by searching for two space-time points with maximum correlation. The assigned velocity is then  $\mathbf{v} = \Delta\mathbf{x}/\Delta t$  where  $\Delta\mathbf{x}$  is the spatial separation of the maximally correlated points and  $\Delta t$  is the time lag. The method is essentially similar to that described in Ref. 51 to analyze experimental GPI data, although some details of the implementation are different. A summary of the method as implemented here is given in Appendix A. The results of the toroidal angular velocity ( $\omega_{\zeta_0}$ ) analysis are shown in Figs. 4 and 5.

Figure 4 shows the radial dependence of  $\omega_{\zeta_0}$  at two different poloidal locations: the midplane and a point just above the X-line. The angular velocity is roughly constant in the region

just inside the separatrix,  $0.98 < \psi < 1.00$  but deviates strongly from that value in the SOL where it also varies with poloidal position. The error bars in the figure indicate the standard deviation of multiple measurements including at various  $\zeta_0$  locations and over different time intervals. (See Appendix A.) In summary the  $\omega_{\zeta_0}$  flow is strongly sheared as a result of both radial and poloidal variation in the SOL. This flow shear accounts for the appearance of the sheared filaments in Fig. 3.

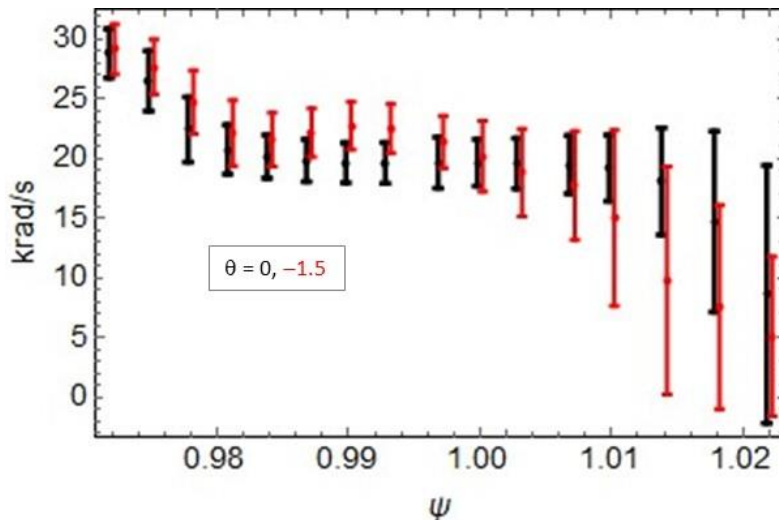


Figure 4. Toroidal angular velocity  $\omega_{\zeta_0}$  of the filaments vs. radial flux coordinate at two different poloidal angles:  $\theta = 0$  (black) corresponding to the outboard midplane and  $\theta = -1.5$  rad (red) corresponding to the lower end of the filament near the X-point line. Note the velocity shear due to radial and poloidal variation, especially in the SOL. Error bars indicate the standard deviation of multiple measurements (see Appendix A).

The parallel variation of  $\omega_{\zeta_0}$  is analyzed in more detail in Fig. 5. Again, it can be seen that the flow is more or less uniform in the central region of the filament, but becomes strongly sheared at both extremities near the top and bottom of the torus, and can even change sign. Part of the reason for the poloidal variation of the flows may be associated with the development of structure in the electrostatic potential near X-points, e.g. caused by X-point losses.<sup>52</sup>

The blobs also move radially, although the radial motion is about two orders of magnitude smaller than the toroidal motion and is therefore rather difficult to detect by the correlation method. We will return to the radial motion in Sec. V.

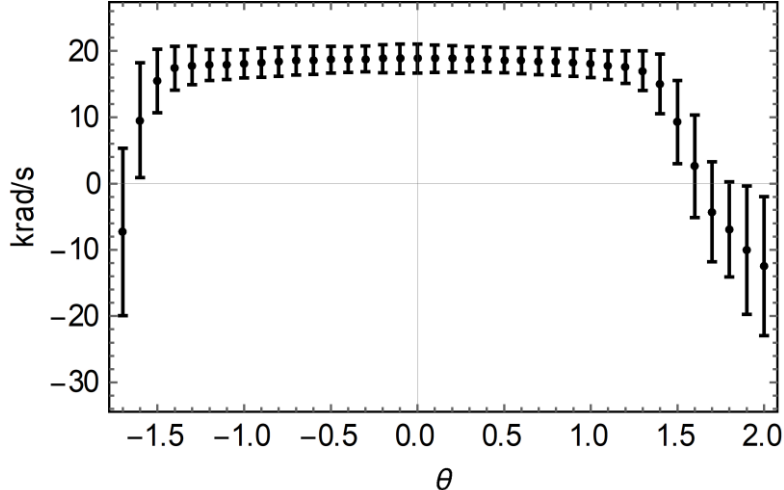


Figure 5. Toroidal angular velocity  $\omega_{\zeta\theta}$  of the filaments vs. poloidal angle on the flux surface  $\psi = 1.01$ . Note the difference in toroidal velocity between the midplane and the lower ( $\theta = -1.5$ ) or upper virtual ( $\theta = 2$ ) X-points. Error bars indicate the standard deviation of multiple measurements (see Appendix A).

## IV. Theory of charge shorting

We have seen that spontaneous poloidally-sheared flows that develop in the plasma, particularly in the SOL and near the X-points (real and virtual) distort the blob-filaments, causing them to depart slightly from the magnetic field lines. Although the departure is only on the order of the blob perpendicular dimensions, perhaps a few millimeters over a meter or more of field line length, it can play a significant role in the dynamics of the structure. Exploring this is the topic of the present section.

### A. Heuristic condition for collisionless kinetic electrons

The basic idea is illustrated in Fig. 6 which shows a field line (black) and a filament which departs from the field line. The sketch is in field line following (FLF) coordinates corresponding qualitatively to Fig. 3. Curvature and  $\nabla B$  drifts charge-polarize the blob-filament in the standard picture of blob dynamics,<sup>1-3</sup> indicated by the red positively charged side of the blob and the blue negatively charged side. If the electron parallel motion along the (black) field line is rapid enough, it will short out the charge polarization. However, the internal charge polarization of the blob is responsible for an internal electric field that propels the blob in the radial direction through its  $E \times B$  drift. Thus, the shorting mechanism enabled by electron parallel conductivity and the parallel shearing of the filament will suppress radial motion of the blob. Essentially, the parallel variation of the filament caused by the sheared flows imposes a  $k_{\parallel}$  on the

filament, making it susceptible to electron conductivity. Some different aspects of a similar mechanism in the presence of *magnetic* shear were also examined in a fluid model in Ref. 53.

The effect of parallel variation of density in a filament and the subsequent development of a Boltzmann response in the electrostatic potential on the blob-filament dynamics was also investigated in a fluid model.<sup>54</sup> The resulting mechanisms discussed therein, namely secondary drift-wave instability of the blob and Boltzmann spinning, are different from the charge shorting mechanism considered here and will be discussed in Sec. VI.

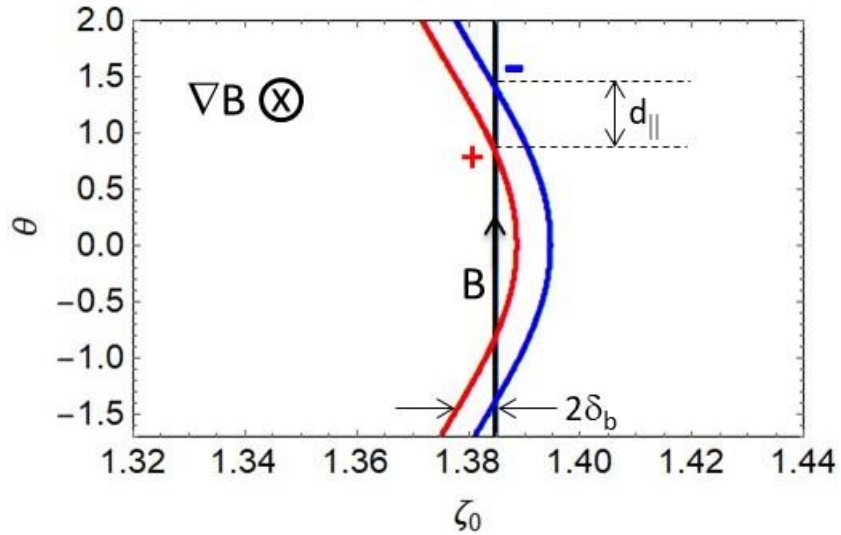


Figure 6. Sketch of a sheared blob filament (red and blue) and magnetic field line (black) in FLF (field line following) coordinates for a particular flux surface. The red and blue lines indicate the two “sides” of a blob of cross-sectional diameter  $2\delta_b$ . The two sides are anchored on different field lines (parametrized by  $\zeta_0$ ), on which positive (red) and negative (blue) polarization charges from curvature and grad-B drifts accumulate. Electrons moving along the field line a parallel distance  $d_{||}$  can short out the charge imbalance.

A heuristic condition for the shorting mechanism to be effective may be obtained by comparing some time scales. Three time scales are of interest, that of (i) parallel electron motion across the sheared filament  $\tau_{e||} = d_{||}/v_{te}$ , (ii) curvature drift of charges across the filament  $\tau_{\kappa} = \delta_b/v_{\kappa}$  and (iii) perpendicular shearing  $\tau_s = \delta_b/v_s$ . Here  $d_{||}$  is the parallel distance between the two sides of the filament (see Fig. 1),  $v_{te}$  is the electron thermal velocity,  $\delta_b$  is the perpendicular blob radius,  $v_{\kappa}$  is the curvature (or grad-B) drift velocity and  $v_s$  is the shearing velocity of the filament, i.e.  $\tau_s$  is the time for the filament to distort by  $\delta_b$  in the frame of its average motion. If  $\tau_{e||} < \tau_{\kappa}$ ,  $\tau_s$  then the charge polarization from curvature and grad-B drifts would be shorted out

before it can build up. Conversely, the charge shorting mechanism is ineffective in the limit  $\tau_{e\parallel} > \tau_K$ . The only other possibility is  $\tau_s < \tau_{e\parallel} < \tau_K$  in which case the filament distorts significantly by sheared flow before the electrons can move. In this case the shorting mechanism is modified because the field line may or may not connect opposite charges any longer, or the filament may break up.

The curvature, or equivalently  $\nabla B$ , drift velocity in a tokamak is estimated as

$$v_K = \frac{cT}{eBR} = \frac{c_s \rho_s}{R} \quad (3)$$

independent of species for  $T_e = T_i = T$ . Here  $c_s = (T_e/m_i)^{1/2}$  is the sound speed and  $\rho_s = c_s/\Omega_i$  is the ion sound radius where  $\Omega_i$  is the ion cyclotron frequency. For a fixed shape of sheared blob-filament like that illustrated in Fig. 6 we have noted above that shorting will occur when  $\tau_{e\parallel} < \tau_K$ . The entire blob-filament can be  $E \times B$  drifting both in the radial and binormal directions. This will have no effect on the shorting mechanism since the electrons drift with the structure. However, if the blob-filament is subject to sheared flows then the structure illustrated in Fig. 6 will distort with time. The relevant shearing velocity is  $v_s = R \Delta\omega_{\zeta_0}$  where  $\Delta\omega_{\zeta_0}$  is the change in toroidal angular velocity over a distance comparable to the parallel scale length of the filament.

Neglecting dynamical shearing for the moment, and assuming the filament is already distorted as shown in Fig. 3, the relevant condition to fulfill for electron shorting of blob propagation in the collisionless kinetic limit is  $\tau_{e\parallel} < \tau_K$  or equivalently  $d_{\parallel}/c_s \rho_s < \delta_b R v_{te}$ . When  $T_i > T_e$  as it is for the blobs in this simulation, the estimate of the curvature velocity in Eq. (3) should be modified by the replacement  $c_s \rho_s \rightarrow v_{ti} \rho_i$ . Thus, a more general condition for charge shorting in the collisionless regime takes the form

$$\frac{d_{\parallel} c_s \rho_s}{R v_{te} \delta_b} \left( 1 + \frac{T_i}{T_e} \right) < 1 \quad (4)$$

The preceding inequality is typically easily satisfied since  $c_s \ll v_{te}$ ,  $\rho_s < \delta_b$  and in the presence of sheared structures  $d_{\parallel} < R$ . This condition, Eq. (4), and importantly the condition for this collisionless estimate to apply, will be compared with simulation parameters in Sec. V.

### ***B. Collisional fluid electrons***

Since most of the previous simulation work on blobs has been done in the context of fluid models, in this section a condition for electron shorting is developed in the collisional fluid limit.

It will be sufficient to consider an isothermal reduced fluid model, as described e.g. in Appendix A of Ref. 55.

In Bohm-normalized variables (i.e. time normalized to  $1/\Omega_i$ , space to  $\rho_s$  and density to a reference density  $n_0$ ), the electrostatic potential and plasma density obey the coupled equations

$$\frac{d}{dt} \nabla \cdot n \nabla \Phi = A_{dw}(\Phi, n) + \alpha_{sh} J_{||sh} - \beta \frac{\partial n}{\partial y} \quad (5)$$

$$\frac{dn}{dt} = A_{dw}(\Phi, n) - \alpha_{sh} (n - J_{||sh}) \quad (6)$$

where the convective derivative is written as  $d/dt = \partial/\partial t + \mathbf{v} \cdot \nabla$  with  $\mathbf{v} = \mathbf{e}_z \times \nabla \Phi$  and  $A_{dw}$  is the adiabatic (drift wave) operator

$$A_{dw}(\Phi, n) = \alpha_{dw} \{ \Phi - \ln n \} \quad (7)$$

$$\alpha_{dw} = \frac{2k_{||}^2 v_{te}^2}{v_{ei0} \Omega_i} \quad (8)$$

Here, for any quantity  $Q$ ,  $\langle Q \rangle \equiv \bar{Q}$  denotes the zonal or y average part and in Eq. (7)  $\{Q\} \equiv Q - \bar{Q}$  denotes the fluctuating part. In the reduced model (x, y) are the radial and binormal variables, and  $\mathbf{B} = B\mathbf{e}_z$ . Thus,  $A_{dw}$  enforces a Boltzmann response on fluctuations when the coefficient  $\alpha_{dw}$  is large, in the spirit of the Wakatani-Hasegawa<sup>56</sup> adiabaticity parameter. Here, the collision frequency  $v_{ei0}$  is based on the reference density.

Other coefficients appearing in the model are: the sheath conductivity parameter  $\alpha_{sh} = \rho_{s0}/L_{||}$  where  $\rho_{s0}$  is the reference sound gyro-radius, and the curvature parameter  $\beta = 2\rho_{s0}/R$  where  $R$  is the effective radius of curvature. In this reduced model, the parallel sheath current  $J_{||sh}$  is ultimately given in terms of  $n$  and  $\Phi$  by closure relations in the sheath-limit and conduction-limited (collisional) regimes.

As is well known, the radial blob velocity  $v_b \sim \partial\Phi/\partial y \sim \Phi/\delta_b$  (in Bohm normalized variables) is obtained from the blob polarization potential  $\Phi$  by balancing either (i) the sheath current  $\alpha_{sh} J_{||}$  in the sheath-connected limit, or (ii) the ion polarization current  $(d/dt) \nabla \cdot n \nabla \Phi \sim \mathbf{v} \cdot \nabla \nabla \cdot n \nabla \Phi \sim n \Phi^2 / \delta_b^4$  in the inertial limit, with the curvature term  $\beta \partial n / \partial y \sim 2n / (R \delta_b)$ .

For a Gaussian shaped blob profile in density,  $n(y)$  is even about the blob centroid and  $\partial n / \partial y$  is odd. This gives rise to an odd or ‘‘dipole’’ potential profile  $\Phi(y) \sim \partial n / \partial y$  which in turn

provides an even poloidal electric field  $\partial\Phi/\partial y$  to propel the radial  $E \times B$  blob propagation. When  $\alpha_{dw}$  is large enough to dominate the vorticity equation, it instead enforces  $\Phi \sim \ln n$ , i.e. an even  $\Phi(y)$  for even  $n(y)$  and no net radial propagation. In the language of turbulence theory, the cross-phase between  $n$  and  $\Phi$  is  $\pi/2$  for small  $\alpha_{dw}$  (high collisionality) which promotes curvature driven radial transport, but the cross-phase tends to 0 for large  $\alpha_{dw}$  (low collisionality, adiabatic electrons) which mitigates that transport channel.

A heuristic condition for adiabatic shorting of the curvature-driven charge polarization in fluid theory is obtained by estimating the potential response arising from Eq. (5)

$$\delta\Phi = \delta n \frac{\alpha_{dw} + ik_y\beta}{\gamma k_{\perp}^2 + \alpha_{dw}} \quad (9)$$

where  $k_y$  and  $k_{\perp}$  are typical inverse spatial scales (blob sizes) and  $\gamma$  is a characteristic inverse blob time scale. Here the sheath term, which is not relevant to this discussion, has been dropped for simplicity. Comparing the curvature and electron parallel streaming terms in the numerator we see that the phase between  $\delta\Phi$  and  $\delta n$  transitions from hydrodynamic-like ( $\delta\Phi \propto ik_y \delta n$ ) to adiabatic-like ( $\delta\Phi \propto \delta n$ ) when  $\alpha_{dw} > k_y\beta$ , or restoring dimensional variables, when

$$\alpha_{dw} > \beta \frac{\rho_s}{\delta_b} \quad (10)$$

At even larger  $\alpha_{dw} \gg \gamma k_{\perp}^2 \gg k_y\beta$ , the transition to adiabatic electrons is complete. Equation (10) can be written in the form

$$\frac{k_{\parallel} v_{te}}{v_{ei}} k_{\parallel} v_{te} R \delta_b > c_s \rho_s \quad (11)$$

Fluid theory, and the above condition, are valid for the electrons in the short mean free path limit  $k_{\parallel} v_{te} < v_{ei}$ . At the validity boundary of the fluid regime  $k_{\parallel} v_{te} \sim v_{ei}$  and identifying  $k_{\parallel} \sim 1/d_{\parallel}$  Eq. (11) agrees, as it should, with the kinetic result given in Eq. (4). Thus, the charge-shortening mechanism should be present in a 3D fluid turbulence simulation, provided the required conditions, including Eq. (11), are satisfied.

## V. Application to the simulation

To decide whether the charge shorting mechanism is active in the XGC1 simulation, we first evaluate the collisionality ratio  $k_{\parallel}v_{te}/v_{ei}$  at the location  $\psi = 1.01$  where the relative fluctuation levels maximize. Employing the parameters  $n_e = 5.6 \times 10^{19} \text{ m}^{-3}$ , electron temperature  $T_e = 40 \text{ eV}$ , ion temperature  $T_i = 155 \text{ eV}$  and  $B = 4.4 \text{ T}$  and taking  $k_{\parallel} = 2\pi/L_{\parallel b}$  where  $L_{\parallel b}$  is the parallel dimension of the blob  $\sim 0.9 \text{ m}$ , we find  $k_{\parallel}v_{te}/v_{ei} \sim 2.4$  which puts the blob in the collisionless kinetic regime. It may also be reasonable to estimate  $k_{\parallel} \sim 1/d_{\parallel}$  where  $d_{\parallel}$ , defined in Fig. 6, is estimated next. This leads to the same conclusion: the blob is at least marginally in the kinetic regime.

A detailed analysis was carried out on the filament shown in Fig. 7. Comparing it with the filaments shown in Fig. 3 also illustrates both the similarity and variability of these structures. The filament shown in Fig. 7 has its centroid at the location of the dashed vertical line at  $\zeta_0 = 1.487$ . From a cut along this line the full width half maximum (FWHM) in the  $\theta$  variable was measured and converted to distance along the connecting field line. This results in the estimate  $d_{\parallel} = 18 \text{ cm}$ . For the same blob-filament, the perpendicular size  $\delta_b$  was measured by converting its half width half maximum (HWHM) in  $\zeta_0$  to an equivalent distance in the binormal direction, yielding  $\delta_b = 0.18 \text{ cm}$ .

Substituting the preceding estimates into Eq. (4) yields  $d_{\parallel}\rho_s c_s (1 + T_i/T_e)/(R\delta_b v_{te}) = 0.002 \ll 1$  indicating that the condition for charge sorting is easily satisfied. However, in this simulation, the filament shearing is sufficiently pronounced that a simple static picture like that implied in Fig. 6 may not apply. For the parameters given in the first paragraph of this subsection one finds  $\tau_{e\parallel} = 0.07 \text{ } \mu\text{s}$  and  $\tau_K \sim 36 \text{ } \mu\text{s}$ . From Fig. 5 we estimate the change in toroidal angular velocity to be on the order of  $\Delta\omega_{\zeta_0} \sim 20$  to  $40 \text{ krad/s}$  resulting in  $\Delta v_{\zeta_0} = R\Delta\omega_{\zeta_0} \sim 18$  to  $36 \text{ km/s}$  and  $\tau_s \sim 0.10$  to  $0.05 \text{ } \mu\text{s}$ . Thus, the simulation is in the regime  $\tau_s \sim \tau_{e\parallel} \ll \tau_K$  where charge shorting should occur, but may be modified or even partly mitigated by dynamical shearing.

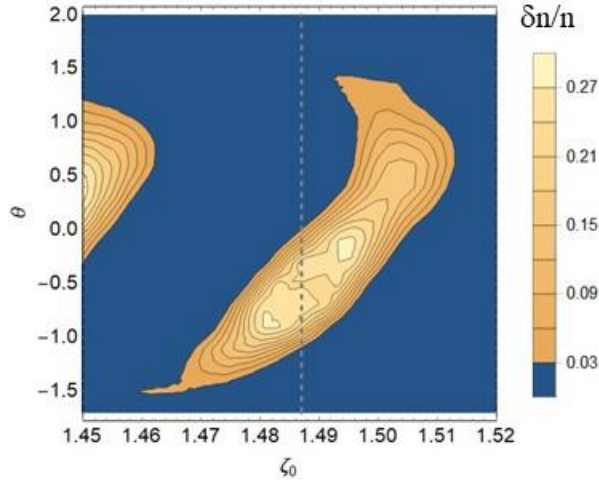


Figure 7. Snapshot showing positive contours of  $\delta n/\bar{n}$  for a blob-filament on the flux surface  $\psi = 1.01$ . The dashed horizontal line passes through the centroid, where the parameter  $d_{||}$  is measured using the FWHM.

These considerations suggest a nearly adiabatic electron density response to potential perturbations. In Fig. 8 the electron density and electrostatic potential are overlaid for a field line in the closed surface region. The electron response is indeed nearly adiabatic. The adiabaticity is even more pronounced in the SOL (not shown) where the curves essentially overlay. This nearly adiabatic response mitigates radial blob propagation. Of course, there may be additional reasons for a nearly adiabatic electron density, including the presence of drift-type turbulence with finite  $k_{||}$ . In the nonlinear state the turbulence and filament shearing are coupled.

To study the actual radial velocity of the structures, several diagnostic methods were employed. First is the time-lag correlation method, described in Sec. III B and in more detail in Appendix A. As explained there, the time-lag correlation method does not provide a very sensitive diagnostic for the radial velocity in these simulations. The resulting radial blob velocities shown as black data points in Fig. 9 come with large standard deviations on the order of 0.5 km/s. The means are nearly zero but show a slight tendency to decrease moving from the closed surface region into the SOL.

A second velocity diagnostic may be referred to as the velocity proxy method. In this method, we do not attempt to diagnose the actual motion of structures from one time to the next but rather look at the average  $E \times B$  velocity  $v_E$  at locations where  $\delta n > 0$ . (See Appendix B for details.) The results are shown in Fig. 9 as a solid black curve which peaks at about 300 m/s in

the closed surface region and drops to nearly zero in the SOL. The same technique may also be applied to only the most positive parts of the structure  $\delta n > \delta n_{th}$  for some positive threshold  $\delta n_{th}$ . As seen in Fig. 10 results are not overly sensitive to  $\delta n_{th}$  but tend to rise somewhat in the edge region as the threshold is raised.

A third method is to measure the blob velocity by a tracking method described in Ref. 40. Briefly, in this method a region of plasma in the  $(R, Z)$  plane with  $\delta n/\bar{n}$  exceeding a threshold (0.1 here) is first identified as a blob in a given frame, i.e. at a given time. A blob with similar features (size, spatial proximity, etc.) is then identified in a subsequent frame and the velocity of the structure is determined directly from its spatial motion in the given time interval. This analysis, applied to 128 frames yielded 629 trackable blobs in the range  $\psi = 1.00$  to 1.01 and 798 trackable blobs in the range  $\psi = 1.01$  to 1.02. Outside of these  $\psi$  intervals, there were too few trackable blobs for a statistically significant result. Results for the mean blob velocity from this analysis are shown as thick blue bars in Fig. 9. Similar to the blob proxy method in the SOL, the blob radial velocities from the tracking method are nearly zero.

The blob tracking code also yields other information about the blob structure. Of particular interest here is the size distribution, which indicates a mean  $\delta_b$  of 0.23 cm, close to the 0.18 cm of the example shown in Fig. 7.

Of course, the different ‘‘blob velocity’’ diagnostics all measure subtly different things. They are not expected to agree in detail. In particular the correlation method is the most sensitive to small structures while the proxy and tracking methods explicitly invoke a threshold on amplitude.

Finally, Fig. 9 shows an analytical estimate of what the blob velocity would be for these parameters in a reduced fluid model where the shorting mechanism is not operative. As shown in Appendix C, the appropriate estimate is from the inertial or RB regime of the two-region model.<sup>24</sup> In this regime the radial blob velocity  $v_b$  is obtained by balancing the ion polarization current  $(d/dt) \nabla \cdot n \nabla \Phi$  (i.e. inertia) with the curvature (charge polarization) term. The inertial regime blob velocity is

$$v_{b,in} \sim c_s \left[ \frac{f_b \delta_b}{R} \left( 1 + \frac{T_i}{T_e} \right) \right]^{1/2} \quad (12)$$

where  $f_b \equiv \delta n/\bar{n}$  is a proxy for the perturbation amplitude. For nominal parameters given in the preceding this evaluates to  $v_{b,in} \sim 1.4$  to 3.2 km/s for  $f_b$  in the range 0.1 to 0.5. A more accurate

evaluation of Eq. (14) using local plasma parameters and corresponding rms values of  $f_b$  is shown as the red curve in Fig. 9. In principle, for pressure driven perturbations, one should take  $f_b \equiv \delta p / \bar{p}$  which could increase  $v_{b,in}$  even further; however, for present purpose the conservative estimate shown in Fig. 9 will suffice.

From these diagnostics and estimates, it can be concluded that the observed blob velocities are indeed much smaller than Eq. (12) would yield were an ideal fluid model applicable. This is consistent with the predicted shorting mechanism.

It is interesting to note that experimentally observed blob velocities in Alcator C-Mod span a range comparable to the scale of Fig. 9. Using a similar correlation technique to that described here, Zweben<sup>51</sup> finds typical radial turbulence velocities for C-Mod in the range 0.1 to < 1 km/s. In different sets of discharges Grulke<sup>57</sup> reported 0.5 to 2 km/s using correlation and tracking, with most structures having  $v_b \sim 0.5$  km/s; Terry<sup>58</sup> finds typical radial turbulence

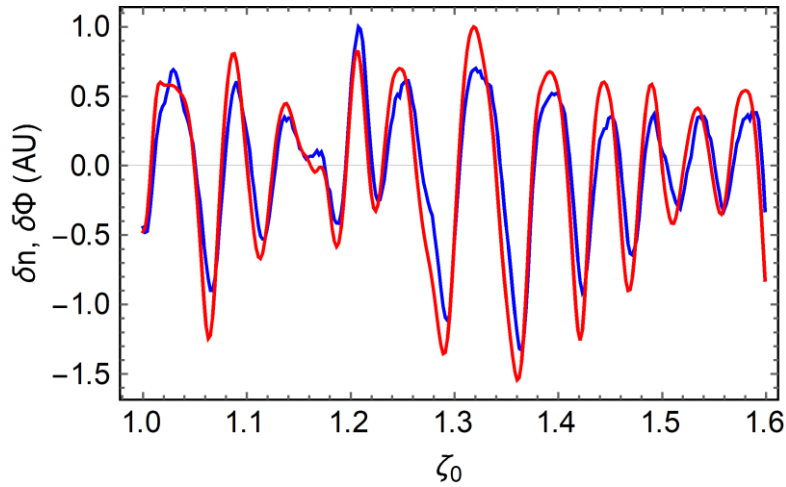


Figure 8. Cross-field variation of normalized density (blue) and potential (red) fluctuations for a range of toroidal field line labels  $\zeta_0$  near the outboard midplane on the flux surface  $\psi = 0.98$ . Curves are normalized to their maximum values for the purpose of superposition.

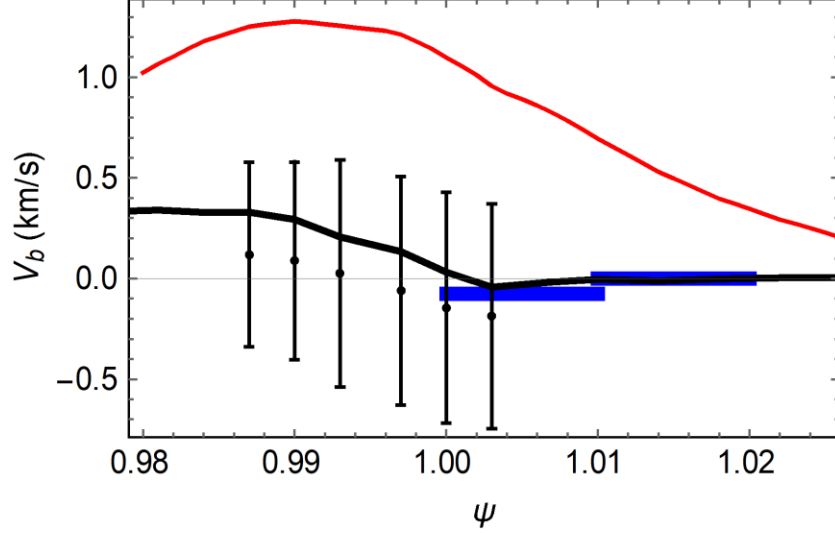


Figure 9. Ideal analytical (red) and gyrokinetic simulation radial blob velocities measured by three techniques (black, blue) at the outboard midplane. The ideal analytical blob velocity is a reduced fluid model estimate appropriate to the inertial (also called resistive ballooning RB) regime in the absence of parallel shearing and electron shorting effects. The solid black curve is obtained using the blob velocity proxy method; the data points with error bars result from applying the correlation method; the blue bars indicate results from the blob tracking method. The reasons for the limited spatial range of the latter two methods is given in the main text and the interpretation of the error bars is discussed in Appendix A.

velocities that are less than 1 km/s. These experimental results are roughly consistent with the XGC1 simulation reported here, although the suppression of blob velocities in the SOL is not as strong in the experiments as in the simulation. We can also speculate that the occasional larger velocities reported experimentally in C-Mod ( $\sim 1$  km/s) may have been filaments that were unaffected by shearing, perhaps because of flow variations throughout the discharge, which is much longer than the  $95 \mu\text{s}$  that could be simulated here.

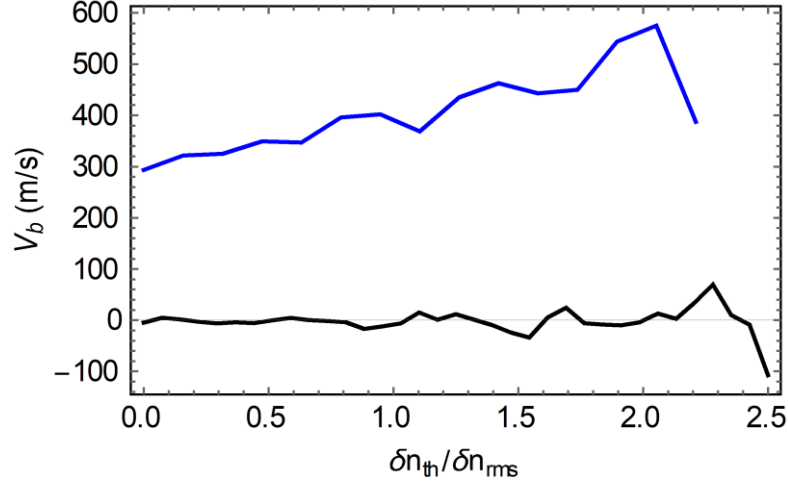


Figure 10. Sensitivity of the blob velocity proxy method to the threshold amplitude  $\delta n_{th}/\delta n_{rms}$ . Results for two different radial positions are shown:  $\psi = 0.99$  (blue) and  $\psi = 1.01$  (black). The poloidal location is at the outboard midplane.

## VI. Discussion

As previously noted, the mechanism for dipole charge shorting that is the main point of Sec. IV, is different from the mitigation of dipole charges by “Boltzmann spinning.”<sup>54</sup> The dipole charge shorting condition, given in the collisionless electron limit by Eq. (4) and for collisional fluid electrons in Eq. (11), is applicable when the filament is not aligned along the magnetic field. In this case the parallel motion of the electrons can respond to the dipole pressure gradient and potential perturbations that are responsible for radial blob convection and thereby slow the convection.

On the other hand, the Boltzmann spinning mechanism is most easily understood when the filament is perfectly aligned along the magnetic field but has a parallel density gradient. Assuming the parallel electric field and parallel pressure gradient terms dominate Ohm’s law, a Maxwell-Boltzmann monopole potential with parallel variation  $\Delta\Phi_l \sim \ln \Delta n$  results (in dimensionless variables assuming isothermal electrons and a parallel filament density variation  $\Delta n$ ). It was shown in Ref. 54 using 3D fluid simulations and analytical analysis that Boltzmann spinning develops under these conditions and mitigates the dipole polarization charges when the monopole potential  $\Phi_l$  exceeds the dipole potential  $\Phi_2$  (within an order unity factor). Boltzmann spinning and polarization charge rotation were also seen in 2D simulations<sup>55</sup> using a model similar to Eqs. (5) and (6).

Other mechanisms can also give rise to spinning, such as a cross-field temperature gradient in sheath-connected blobs,<sup>59</sup> resulting in the same effect (reduction of radial velocity and a transfer of radial velocity to the poloidal component). While this particular mechanism is not directly relevant here because the blobs are electrically disconnected from the sheaths, any cross-field process that links the perpendicular electrostatic potential and temperature or density gradients would also have an analogous effect.

The simultaneous effects of dipole charge shorting for poloidally sheared filaments and spinning have not been studied, but it is clear that blob-filament spinning occurs whenever the electron response allows a monopole potential, and that the mitigation condition  $\Phi_1 > \Phi_2$  should be more easily satisfied if  $\Phi_2$  has been reduced by charge shorting. Thus, there may be synergistic effects. Indeed, in the simulation under study, any charges not mitigated by the shorting mechanism would be mitigated by Boltzmann spinning since it can be seen from Fig. 8 that the Boltzmann contribution dominates the total potential.

Ideally the effects of charge shorting on blob motion would best be quantified by comparing simulation results with and without sheared flows satisfying Eq. (4), but with other conditions unchanged as much as possible. This would account for mechanisms in addition to charge shorting that could slow the blob motion. For example, one caveat of our analysis is that neutrals were present in the analyzed simulation; they could in principle affect the blob velocity through charge-exchange friction. The large computation expense of running the XGC1 code has so far made such direct comparative runs impractical. Shorter seeded-blob simulations are presently under investigation for this purpose.

Although the dynamics of filaments that are sheared by poloidally varying toroidal flows were studied in the present paper using results from a gyrokinetic simulation, the phenomena of poloidally shearing and charge shorting should in principle be accessible to fluid codes in the appropriate parameter regime. Specifically, Eq. (11) must be satisfied, which in practice is usually easy, even in the strongly collisional plasmas required for the validity of fluid models. However, for marginally collisional SOL plasmas, it is well known that fluid models may be subject to some inaccuracies in the electron parallel response, and the representation of charge shorting would be more qualitative. Also, some mechanisms for generating sheared flows such as direct particle loss, may not be present.

In this paper we have not addressed the causes for the observed poloidally varying toroidal flows. This is certainly an interesting question, but one which is well beyond the scope

of this paper. We speculate that X-point ion losses, neoclassical physics, turbulence physics and the transition from closed to open field lines are involved. All of these likely play in role in establishing the electrostatic potential in the edge and SOL regions. Some aspects of the interplay among these mechanisms has been discussed in other works, both for XGC1<sup>14,40,52</sup> and fluid turbulence codes.<sup>47,60</sup>

## VII. Summary and conclusions

The primary results of this paper are to be found in Eqs. (4) and (11) and Figs. 3 – 6 and in Fig. 9. Figure 3 visually illustrates the shearing of blob-filaments within a flux surface in the gyrokinetic simulation. It is caused by poloidal (parallel) variation of toroidal flows. The filament shearing is quantified in Figs. 4 and 5 where it is shown that the shearing is largest near X-points and in the scrape-off layer. Conversely, shearing is smallest near the outboard midplane and in the closed surface region just inside the separatrix. The causes for these flow patterns are outside the scope of this paper. Rather, the focus of the paper is on the consequences of such flows, when they occur, on filament shearing and radial propagation. Our focus on the consequences of filament shearing on blob propagation is not meant to imply the absence of other, possibly synergistic or competing mechanisms relevant to blob propagation.

The sketch in Fig. 6 illustrates the fundamental mechanism of charge shorting by parallel electron currents when a filament is sheared by the parallel variation of toroidal flows. This effectively generates a  $k_{\parallel}$  which enhances the role of the electrons and enables the electron response to approach an adiabatic response. Analytical conditions for when the shorting mechanism is applicable are given for the collisionless kinetic electron limit in Eq. (4) and for collisional fluid theory in Eq. (11). Figure 9 compares the blob velocities diagnosed from the simulation with an analytical estimate of what those velocities would be from an ideal fluid model in the absence of the shorting mechanism. The shorting mechanism inhibits charge polarization of the blob-filament and therefore inhibits the mechanism by which blobs are propelled radially, slowing them down as observed in the simulation. The resulting blob velocities were also found to be broadly consistent with experimental observations.

While simple scaling arguments like those proposed in the original two-region model<sup>24</sup> and related models<sup>25</sup> give definite values for the blob velocity for given plasma parameters, experimentally and in codes a statistical distribution of blob radial velocities is invariably observed.<sup>5-7</sup> One reason for this is that the velocity depends on blob size,  $\delta_b$ , and the turbulence

generates a statistical distribution of sizes. Given the present study, it is also of interest to speculate that another reason for the distribution of blob velocities is that the blob-filaments are subject to sheared flows which may vary throughout a discharge in space and time, on longer time scales than could be simulated here. Blob-filaments may be influenced differently by the charge shorting mechanism depending on the background sheared flows they encounter.

It is possible that the shearing mechanism could be deliberately employed to control blob velocities by biasing. Biasing has been tried experimentally with some success,<sup>61</sup> motivated by other theoretical considerations.<sup>62</sup> Strongly sheared flows in the SOL may already be present due to self-biasing in experiments which apply RF waves in the ion-cyclotron range of frequencies (ICRF).<sup>46,63,64</sup>

In closing, we emphasize that it will be important to continue studies of kinetic and fluid effects on blob-filament dynamics in order to better understand and predict the impact of these turbulent structures on the near-SOL width and on main chamber wall interactions in the far SOL.

## Acknowledgements

This material is based upon work supported by the U.S. Department of Energy Office of Science, Office of Fusion Energy Sciences under Award Number DE-AC02-09CH11466 sub-contract SO15882-C and US DOE Grant DE-FC02-99ER54512, using Alcator C-Mod, a DOE Office of Science User Facility. We thank J. Hughes for providing the Alcator C-Mod geometry and profile data. Discussions with members of the HBPS SciDAC project (Scientific Discovery through Advanced Computing Initiative: High Fidelity Boundary Plasma Simulation) are gratefully acknowledged. We acknowledge the use of computing resources on Titan at the Oak Ridge Leadership Computing Facility at the Oak Ridge National Laboratory through the ALCC (ASCR Leadership Computing Challenge) program administered by the U.S. DOE Office of Science. The digital data for this paper can be found in Ref. 65. Additional data that support the findings of this study are available from the corresponding author upon reasonable request.

## Appendix A: Time-lag correlation method

The correlation method provides a measure of the velocity of structures by searching for two space-time points with maximum correlation. The assigned velocity is then  $v = \Delta x / \Delta t$  where

$\Delta \mathbf{x}$  is the spatial separation of the points and  $\Delta t$  is the time lag. However, many detailed considerations enter the actual implementation of this rather simple idea.

The correlation function for the density perturbation  $\delta n$  is defined by

$$C_{\delta n}(\mathbf{x}; \Delta t, \Delta \mathbf{x}) = \frac{\sum_{t=t_1}^{t_2-\Delta t} \delta n(t, \mathbf{x}) \delta n(t + \Delta t, \mathbf{x} + \Delta \mathbf{x})}{\left[ \sum_{t=t_1}^{t_2-\Delta t} \delta n(t, \mathbf{x})^2 \right]^{1/2} \left[ \sum_{t=t_1}^{t_2-\Delta t} \delta n(t + \Delta t, \mathbf{x} + \Delta \mathbf{x})^2 \right]^{1/2}} \quad (\text{A1})$$

where the data record starts at  $t = t_1$  and stops at  $t = t_2$ . First, we choose a time delay that is a multiple of  $\delta t$ , the time resolution of the data set, i.e.  $\Delta t = n \delta t$  where  $n$  is an integer parameter. Then for a given  $\mathbf{x}$ , the maxima of  $C$  must be located within a given search box. The  $n = 1$  search box is chosen to contain a typical blob as it moves with one  $\delta t$  step. The choice of initial box requires some judgment and experimentation; it is not unique. Typical values used include data up to  $\pm 3$  spatial grid-points from the reference location. Have determined the initial ( $n = 1$ ) box, for  $n$  larger than 1, the box is expanded by a factor of  $n$ , so that blobs do not escape the search box. Thus, the correlation velocities so determined depend on the numerical parameters  $n$  and the search box dimensions. Different choices offer competing advantages in terms of velocity scale and resolution.

The velocity resolution is limited by the spatial resolution of the simulation and the largest  $\Delta t$  that can be accommodated without using an unduly large search box. The smallest velocity that can be detected is

$$v_{\min} = \min(\Delta \mathbf{x}) / \Delta t \quad (\text{A2})$$

where  $\Delta x$  is the grid (or node) spacing. If  $\Delta t$  is made large to improve resolution, then either some fast velocities will be missed, or the search box must be increased to the point where adequate spatial resolution and spatial range are lost, the latter because the search box begins to overlap the boundary of the domain.

In the present application  $\mathbf{x}$  may be interpreted as an abstract vector in FLF coordinates,  $\mathbf{x} = (\psi, \zeta_0)$ . Since the fluctuations are statistically independent of the toroidal coordinate  $\zeta_0$ , velocities may be determined for a sequence of toroidal positions. In Figs. 4, 5 and 8 we show the mean and standard deviations over  $\zeta_0$  and  $n = 1, \dots, n_{\max}$  where the standard deviations are plotted as error bars. Typically, we found good results for  $n_{\max}$  in the range 3 to 5.

The method yields good results for the toroidal velocity because the toroidal resolution in FLF coordinates is very good and, because of periodicity, the search boxes never encounter a domain boundary. On the other hand, the method does not work so well for the radial velocity. The first issue is that the radial velocity is much smaller than the toroidal velocity making an optimal choice of  $\Delta t$  for simultaneous measurement of both difficult. This was mitigated by transforming the data into a frame rotating toroidally with the mean toroidal velocity. The second issue is that the radial resolution of the data limits the radial velocity resolution for the reasons just stated to about 1 km/s, and this only over the middle of the radial domain, where boundary issues do not interfere with the calculation.

## Appendix B: Blob velocity proxy method

In this method the blob velocities are not determined by direct detection of their motion but rather it is assumed that the plasma moves radially across field lines at the local  $E \times B$  velocity. Because the  $E \times B$  velocity can have spatial variation on the scale of the blob itself (see e.g. Fig. 7) an appropriate average velocity must be defined. Here we define the blob velocity proxy as

$$v_b(\delta n_{th}) = - \frac{\left\langle H(\delta n - \delta n_{th}) \frac{\partial \delta \Phi}{\partial \zeta_0} \right\rangle}{RB_p \langle H(\delta n - \delta n_{th}) \rangle} \quad (\text{B1})$$

where  $H$  is the Heavyside step function,  $\delta n_{th}$  is a threshold fluctuation level,  $B_p$  is the poloidal magnetic field and the radial  $E \times B$  velocity in FLF coordinates is given by

$$v_{E\psi} = \frac{1}{B^2} \mathbf{e}_\psi \cdot \mathbf{B} \times \nabla \Phi = - \frac{1}{RB_p} \frac{\partial \Phi}{\partial \zeta_0} \quad (\text{B2})$$

An approximation has been made in the final form of Eq. (B2): the contribution of the parallel variation  $\propto \partial \Phi / \partial \theta$  in FLF coordinates is assumed to be negligible, specifically

$$\left| \frac{B_\zeta |\nabla \theta|}{B^2} \frac{\partial \Phi}{\partial \theta} \right| \ll \left| \frac{1}{RB_p} \frac{\partial \Phi}{\partial \zeta_0} \right| \quad (\text{B3})$$

(In principle,  $\partial\Phi/\partial\theta/FLF$  makes a contribution to  $v_{E\psi}$  because the poloidal electric field in geometric angle coordinates  $(\psi, \theta, \zeta)$  is expressed in terms of both  $\partial\Phi/\partial\zeta_0$  and  $\partial\Phi/\partial\theta$  in FLF coordinates.)

The blob velocity proxy given by Eq. (B1) averages  $v_{E\psi}$  over that part of the blob for which the fluctuating density exceeds a threshold value,  $\delta n > \delta n_{th}$ . Thus for  $\delta n_{th} = 0$  the average is taken over all locations with positive fluctuations (“blobs”). As  $\delta n_{th}$  increases, the computed proxy velocity typically increases, as shown in Fig. 9. At large  $\delta n_{th} / \delta n_{rms}$  the statistics become poor.

## Appendix C: Two-region model estimates

It should be kept in mind that the two-region model is rather rudimentary in its representation of X-point geometry, and while useful for understanding blob velocity scaling laws, it is not expected to give accurate order-unity coefficients in those scaling laws or in the regime boundaries. Nevertheless, it is useful to understand the model’s implications.

The fundamental parameters of the two-region model are

$$\Lambda = \frac{v_{ei} L_{||}}{\Omega_e \rho_s} \quad (C1)$$

$$\Theta = \frac{\delta_b^{5/2} R^{1/2}}{\rho_s^2 L_{||}} \quad (C2)$$

and the X-point geometry factor  $\varepsilon_x$ . Here  $L_{||}$  is the midplane to divertor connection length  $\sim 8$  m,  $R \sim 0.89$  m is the major radius, and in the X-point region on the  $\psi = 1.01$  flux surface, we estimate  $\varepsilon_x$  from the flux expansion ratio  $\varepsilon_x \sim RB_p(\text{X-pt})/RB_p(\text{midplane}) \sim 0.1$ . Blob and plasma parameters in the SOL from the simulation give  $n_e \sim 5.6 \times 10^{19} \text{ m}^{-3}$ ,  $T_e \sim 40$  eV,  $T_i \sim 155$  eV,  $B = 4.3$  T, and  $\delta_b \sim 0.18$  cm resulting in  $\Lambda \sim 0.4$ ,  $\Theta \sim 0.4$ . This places the blobs on the RB-RX boundary,  $\Lambda = \Theta$ , where the blob velocity is estimated from the RB scaling as

$$v_b \sim c_s \left( \frac{f_b \delta_b}{R} \right)^{1/2} \quad (C3)$$

Taking  $f_b \sim 0.1$  yields  $v_b \sim 0.6$  km/s similar to Fig. 9 in the SOL. Equation (12) adds the additional curvature drive weighting from finite  $T_i$ . Of course, on the RB-RX boundary the RX scaling will give the same result as Eq. (C3).

The parallel structure of the mode is broadly consistent with these findings. The rms fluctuation level at  $\psi = 1.01$  decays to half of its maximum value at  $\theta = -1.20$  and  $\theta = +1.07$  in FLF coordinates. At these locations the factor  $\varepsilon_x$  defined in the two-region model is respectively 0.88 and 0.95, hardly different from its midplane value of 1. Thus, the filaments do not experience significant X-point effects such as enhanced inertia and are disconnected from the divertor. This eliminates the relevance of the connected-interchange (CI) regime and the sheath-connected (CS) regime, as expected since the CI regime requires  $\Lambda < \varepsilon_x \Theta$ , and CS regime requires  $\varepsilon_x \Theta > 1$ . In the simulations, however, the parallel decay and disconnection of the filaments may be assisted by effects other than resistivity, e.g. shearing by the poloidal variation of the background flows.

## References

- <sup>1</sup> S.I. Krasheninnikov, Phys. Lett. A **283**, 368 (2001).
- <sup>2</sup> S.I. Krasheninnikov, D.A. D’Ippolito and J.R. Myra J. Plasma Phys. **74** 679–717 (2008).
- <sup>3</sup> D. A. D’Ippolito, J. R. Myra, and S. J. Zweben, Phys. Plasmas **18**, 060501 (2011).
- <sup>4</sup> S. J. Zweben, Phys. Fluids **28**, 974 (1985).
- <sup>5</sup> S. J. Zweben, J. R. Myra, W. M. Davis, D. A. D’Ippolito, T. K. Gray, S. M. Kaye, B. P. LeBlanc, R. J. Maqueda, D. A. Russell, D. P. Stotler and the NSTX-U Team, Plasma Phys. Control. Fusion **58**, 044007 (2016).
- <sup>6</sup> J. A. Boedo, D. L. Rudakov, R. A. Moyer, G. R. McKee, R. J. Colchin, M. J. Schaffer, P. G. Stangeby, W. P. West, S. L. Allen, T. E. Evans, et al., Phys. Plasmas **10**, 1670 (2003).
- <sup>7</sup> C. K. Tsui, J. A. Boedo, J. R. Myra, B. Duval, B. Labit, Phys. Plasmas **25**, 072506 (2018).
- <sup>8</sup> F. Scotti, S. J. Zweben, J. R. Myra, V. Soukhanovskii, R. Maqueda, M. Jaworski, Nucl. Fusion **60**, 026004 (2020).
- <sup>9</sup> G. Fuchert, G. Birkenmeier, D. Carralero, T. Lunt, P. Manz, H. W. Müller, B. Nold, M. Ramisch, V. Rohde, U. Stroth, and the ASDEX Upgrade Team, Plasma Phys. Control. Fusion **56**, 125001 (2014).
- <sup>10</sup> J.L. Terry, S. Ballinger, D. Brunner, B. LaBombard, A.E. White and S.J. Zweben, Nucl. Mater. and Energy **12**, 989 (2017).
- <sup>11</sup> C. S. Chang, S. Ku, A. Loarte, V. Parail, F. Koechl, M. Romanelli, R. Maingi, J.-W. Ahn, T. Gray, J. Hughes et al., Nucl. Fusion **57**, 116023 (2017).
- <sup>12</sup> Z. Li, X. Xu, N. Li, V.S. Chan and X. Wang, Nucl. Fusion **60**, 029502 (2020).
- <sup>13</sup> F. D. Halpern, J. Horacek, R. A. Pitts, and P. Ricci, Plasma Phys. Controlled Fusion **58**, 084003 (2016).

- <sup>14</sup> I. Keramidias Charidakos, J. R. Myra, S. Parker, S. Ku, R. M. Churchill, R. Hager and C. S. Chang, *Phys. Plasmas* **25**, 072306 (2018).
- <sup>15</sup> R.A. Pitts, X. Bonnin, F. Escourbiac, H. Frerichs, J.P. Gunn, T. Hirai, A.S. Kukushkin, E. Kaveeva, M.A. Miller, D. Moulton et al., *Nucl. Mater. and Energy* **20**, 100696 (2019).
- <sup>16</sup> D. A. Russell, D. A. D'Ippolito, J. R. Myra, J. M. Canik, T. K. Gray, and S. J. Zweben, *Phys. Plasmas* **22**, 092311 (2015).
- <sup>17</sup> J. R. Myra, D. A. D'Ippolito, and D.A. Russell, *Phys. Plasmas* **22**, 042516 (2015).
- <sup>18</sup> D. Carralero, M. Siccinio, M. Komm, S.A. Artene, F.A. D'Isa, J. Adamek, L. Aho-Mantila, G. Birkenmeier, M. Brix, G. Fuchert, et al., *Nucl. Fusion* **57**, 056044 (2017).
- <sup>19</sup> N. Vianello, D. Carralero, C.K. Tsui, V. Naulin, M. Agostini, I. Cziegler, B. Labit, C. Theiler, E. Wolfrum, D. Aguiam, et al., *Nucl. Fusion* **60**, 016001 (2020).
- <sup>20</sup> A. Wynn, B. Lipschultz, I. Cziegler, J. Harrison, A. Jaervinen et al., *Nucl. Fusion* **58**, 056001 (2018).
- <sup>21</sup> F. Militello and J. T. Omotani, *Plasma Phys. Control. Fusion* **58**, 125004 (2016).
- <sup>22</sup> R. Kube, O. E. Garcia, and M. Wiesenberger, *Phys. Plasmas* **23**, 122302 (2016).
- <sup>23</sup> M. Wiesenberger, M. Held, R. Kube, and O. E. Garcia, *Phys. Plasmas* **24**, 064502 (2017).
- <sup>24</sup> J. R. Myra, D.A. Russell and D. A. D'Ippolito, *Phys. Plasmas* **13**, 112502 (2006).
- <sup>25</sup> P. Paruta, C. Beadle, P. Ricci and C. Theiler, *Phys. Plasmas* **26**, 032302 (2019).
- <sup>26</sup> Y. Sarazin and P. Ghendrih, *Phys. Plasmas* **5**, 4214 (1998).
- <sup>27</sup> D. A. Russell, J. R. Myra and D. A. D'Ippolito, *Phys. Plasmas* **14**, 102307 (2007).
- <sup>28</sup> O. E. Garcia, J. Horacek, R. A. Pitts, A. H. Nielsen, W. Fundamenski, V. Naulin, and J. J. Rasmussen, *Nucl. Fusion* **47**, 667 (2007).
- <sup>29</sup> N. Bisai, A. Das, S. Deshpande, R. Jha, P. Kaw, A. Sen, and R. Singh, *Phys. Plasmas* **11**, 4018 (2004).
- <sup>30</sup> J. R. Angus and M. V. Umansky, *Phys. Plasmas* **21**, 012514 (2014).
- <sup>31</sup> L. Easy, F. Militello, J. Omotani, N. R. Walkden, and B. Dudson, *Phys. Plasmas* **23**, 012512 (2016).
- <sup>32</sup> N. R. Walkden, L. Easy, F. Militello and J. T. Omotani, *Plasma Phys. Control. Fusion* **58**, 115010 (2016).
- <sup>33</sup> F. Riva, F. Militello, S. Elmore, J. T. Omotani, B. Dudson, N. R. Walkden and the MAST team, *Plasma Phys. Control. Fusion* **61**, 095013 (2019).
- <sup>34</sup> P. Paruta, P. Ricci, F. Riva, C. Wersal, C. Beadle and B. Frei, *Phys. Plasmas* **25**, 112301 (2018).
- <sup>35</sup> B. Zhu, M. Francisquez, and B. N. Rogers, *Phys. Plasmas* **24**, 055903 (2017).
- <sup>36</sup> F. Nespoli, P. Tamain, N. Fedorczak, G. Ciraolo, D. Galassi, R. Tatali, E. Serre, Y. Marandet, H. Bufferand and Ph. Ghendrih, *Nucl. Fusion* **59**, 096006 (2019).
- <sup>37</sup> H. Hasegawa and S. Ishiguro, *Phys. Plasmas* **26**, 062104 (2019).
- <sup>38</sup> T. N. Bernard, E. L. Shi, K. W. Gentle, A. Hakim, G. W. Hammett, T. Stoltzfus-Dueck, and E. I. Taylor, *Phys. Plasmas* **26**, 042301 (2019).
- <sup>39</sup> R. M. Churchill, C. S. Chang, S. Ku and J. Dominski, *Plasma Phys. Control. Fusion* **59**, 105014 (2017).
- <sup>40</sup> I. Keramidias Charidakos, J. R. Myra, S. Ku, R.M. Churchill, R. Hager, C.S. Chang and S. Parker, "Comparison of edge turbulence characteristics between DIII-D and C-Mod simulations with XGC1" (accepted for publication in *Phys. Plasmas*, 2020).
- <sup>41</sup> C. S. Chang, S. Ku, G. R. Tynan, R. Hager, R. M. Churchill, I. Cziegler, M. Greenwald, A. E. Hubbard, and J.W. Hughes, *Phys. Rev. Lett.* **118**, 175001 (2017).

- <sup>42</sup> S. Ku, R. Hager, C. Chang, J. Kwon, and S. Parker, *J. Comput. Phys.* **315**, 467 (2016).
- <sup>43</sup> P. W. Terry, *Rev. Mod. Phys.* **72**, 109 (2000).
- <sup>44</sup> P. H. Diamond, S.-I. Itoh, K. Itoh and T. S. Hahm, *Plasma Phys. Control. Fusion* **47**, R35 (2005).
- <sup>45</sup> K. H. Burrell, *Phys. Plasmas* **4**, 1499 (1997).
- <sup>46</sup> W. Zhang, I. Cziegler, V. Bobkov, G.D. Conway, G. Fuchert, M. Griener, O. Kardaun, P. Manz, J.-M. Noterdaeme, E. Seliunin, E. Wolfrum and the ASDEX Upgrade Team, *Nucl. Fusion* **59**, 074001 (2019).
- <sup>47</sup> F. Nespoli, P. Tamain, N. Fedorczak, D. Galassi and Y. Marandet, *Nucl. Fusion* **60**, 046002 (2020).
- <sup>48</sup> J.W. Hughes, P.B. Snyder, M.L. Reinke, B. LaBombard, S. Mordijck, S. Scott, E. Tolman, S.G. Baek, T. Golfinopoulos, R.S. Granetz, M. Greenwald, A.E. Hubbard, E. Marmor, J.E. Rice, A.E. White, D.G. Whyte, T. Wilks and S. Wolfe, *Nucl. Fusion* **58** 112003 (2018).
- <sup>49</sup> S.E. Parker, R.J. Procassini, C.K. Birdsall and B.I. Cohen, *J. Computational Phys.* **104**, 41 (1993).
- <sup>50</sup> D.P. Stotler, J. Lang, C.S. Chang, R.M. Churchill and S. Ku, *Nucl. Fusion* **57**, 086028 (2017).
- <sup>51</sup> S. J. Zweben, J. L. Terry, B. LaBombard, M. Agostini, M. Greenwald, O. Grulke, J. W. Hughes, D. A. D'Ippolito, S. I. Krasheninnikov, J. R. Myra, D. A. Russell, D. P. Stotler, M. Umansky, *J. Nucl. Mater.* **415**, S463 (2011).
- <sup>52</sup> C.S. Chang, S. Ku, and R.M. Churchill, *Phys. Plasmas* **26**, 014504 (2019).
- <sup>53</sup> A. A. Stepanenko, W. Lee, and S. I. Krasheninnikov, *Phys. Plasmas* **24**, 012301 (2017).
- <sup>54</sup> J. R. Angus, S. I. Krasheninnikov and M. V. Umansky, *Phys. Plasmas* **19**, 082312 (2012).
- <sup>55</sup> J.R. Myra, W.M. Davis, D.A. D'Ippolito, B. LaBombard, D.A. Russell, J.L. Terry and S.J. Zweben, *Nucl. Fusion* **53**, 073013 (2013).
- <sup>56</sup> M. Wakatani and A. Hasegawa *Phys. Fluids* **27**, 611 (1984).
- <sup>57</sup> O. Grulke, J. L. Terry, B. LaBombard and S. J. Zweben, *Phys. Plasmas* **13**, 012306 (2006).
- <sup>58</sup> J.L. Terry, S.J. Zweben, O. Grulke, M.J. Greenwald, B. LaBombard, *J. Nucl. Mater.*, **337–339**, 322 (2005).
- <sup>59</sup> J. R. Myra, D. A. D'Ippolito, S. I. Krasheninnikov and G.Q. Yu, *Phys. Plasmas* **11**, 4267 (2004).
- <sup>60</sup> D. Galassi, P. Tamain, H. Bufferand, G. Ciralo, P. Ghendrih, C. Baudoin, C. Colin, N. Fedorczak, N. Nace, and E. Serre, *Nucl. Fusion* **57**, 036029 (2017).
- <sup>61</sup> S. J. Zweben, M. D. Campanell, B. C. Lyons, R. J. Maqueda, Y. Raiteses, A. L. Roquemore, F. Scotti and H. Takahashi, *Plasma Phys. Control. Fusion* **54**, 105012 (2012).
- <sup>62</sup> R. H. Cohen and D. D. Ryutov, *Nucl. Fusion* **37**, 621 (1997).
- <sup>63</sup> I. Cziegler, J. L. Terry, S. J. Wukitch, M. L. Garrett, C. Lau and Y. Lin, *Plasma Phys. Control. Fusion* **54**, 105019 (2012).
- <sup>64</sup> D. A. D'Ippolito, J. R. Myra, J. Jacquinet and M. Bures, *Phys. Fluids B* **5**, 3603 (1993).
- <sup>65</sup> J. R. Myra, S. Ku, D.A. Russell, J. Cheng, I. Keramidis Charidakos, S. E. Parker, R.M. Churchill, and C.S. Chang, "Reduction of blob-filament radial propagation by parallel variation of flows: analysis of a gyrokinetic simulation," Dataset, (Zenodo, 2020) <https://doi.org/10.5281/zenodo.3770527>

This report was prepared as an account of work sponsored by an agency of the United States Government. Neither the United States Government nor any agency thereof, nor any of their employees, makes any warranty, express or implied, or assumes any legal liability or responsibility for the accuracy, completeness, or usefulness of any information, apparatus, product, or process disclosed, or represents that its use would not infringe privately owned rights. Reference herein to any specific commercial product, process, or service by trade name, trademark, manufacturer, or otherwise does not necessarily constitute or imply its endorsement, recommendation, or favoring by the United States Government or any agency thereof. The views and opinions of authors expressed herein do not necessarily state or reflect those of the United States Government or any agency thereof.